RESEARCH PAPER

Multiple magnetic phase transition and short-range ferromagnetic behavior influence on magnetocaloric effect of Sm$_2$NiMnO$_6$ nanoparticles

I. Phebe Kokila · P. Sathish Kumar · M. Kanagaraj · Anil Kumar Paidi · Liang He · S. Madeswaran · Helen Annal Therese (iD)

Abstract Structural characteristics and magnetocaloric effect of Sm$_2$NiMnO$_6$ double perovskite oxide nanoparticles synthesized via the solution combustion technique have been investigated. From the X-ray structural study, it is found that the Sm$_2$NiMnO$_6$ compound crystallizes in the monoclinic structure ($P2_1/n$ space group), where Ni and Mn atoms are ordered at 2c and 2d sites, respectively. Transmission electron microscopic image reveals agglomerated nanoparticles with an average particle size of 60 nm. Two magnetic Curie transition points (T_{C1} = 141 K, T_{C2} = 67 K) observed from the isofield magnetization measurement affirmed the short-range ferromagnetic behavior of Sm$_2$NiMnO$_6$ creating the continuous second-order transition followed by the discontinuous first-order transition. A minor cusp at 10 K confirmed the microscopic superparamagnetic behavior at low fields apart from the dual magnetic phase transition. Adiabatic demagnetization of Sm$_2$NiMnO$_6$ nanoparticles was measured in terms of magnetic entropy, and the magnetic refrigerant capacity was calculated to be 0.44 J kg^{-1} K^{-1} and ~ 20 J kg^{-1} respectively.

Keywords Magnetically ordered materials · Chemical synthesis · Magnetocaloric · Magnetic measurements · Perovskite · Nanomaterials

I. P. Kokila
Nanotechnology Research Centre, SRM Institute of Science and Technology, Kattankulathur, Chengalpattu, Tamil Nadu 603203, India

P. S. Kumar · S. Madeswaran
Department of Physics, School of advanced sciences, VIT, Vellore 632014, India

M. Kanagaraj
School of Electronic Science and Engineering, Nanjing University, Nanjing 210093, People's Republic of China

A. K. Paidi
Department of Metallurgical Engineering and Materials Science, Indian Institute of Technology (IIT) Bombay, Mumbai 400076, India

L. He
York-Nanjing Joint Center for Spintronics and Nano Engineering (YNJC), School of Electronics Science and Engineering, Nanjing University, Nanjing 210093, People's Republic of China

H. A. Therese (✉)
Department of Chemistry, SRM Institute of Science and Technology, Kattankulathur, Chengalpattu, Tamil Nadu 603203, India
e-mail: helena@srmist.edu.in

Introduction

Modern solid-state cooling technology transcends the volatile liquid refrigerant–based conventional cooling system as it is inclined on offering higher working efficiency which helps in the conservation of energy. Solid-state cooling technologies involves the magnetocaloric, electrocaloric, elastocaloric, and barocaloric effects found in advanced novel caloric materials. Among these, magnetocaloric cooling has well developed over the years, bringing the technology for practical applications such as in heat pumps, centralized air conditioners, liquor distillation process, waste

purification, magnetic hyperthermia, and helium lique-faction (Chakraborty et al. 2017a; Kotnana et al. 2018). The refrigeration capacity (RC), magnetic entropy change (ΔS_M), and adiabatic temperature range have been evaluated by three distinctive factors such as temperature, magnetic field, and external pressure (Takeuchi and Sandeman 2015). These key parameters are used to correlate each other to evaluate the refrigeration capacity of the magnetocaloric material, which are derived from the variation of magnetic entropy change by external pressure and applied magnetic field. The cooling technology requires materials with high magnetic refrigeration capacity along with a large magnetic moment such as $Gd_5(Si_2Ge_2)$, $MnAs_{1-x}Sb_x$, ErNiBC, and GdNiBC respectively (Romero Gómez et al. 2013). Apart from the materials that exhibit high magnetic refrigeration capacity, the double perovskite materials still need to be explored to find their magnetocaloric properties and tuned for attaining higher refrigeration capacity (El Kossi et al. 2015). Previous reports demonstrated a giant magnetocaloric effect on gadolinium-based double perovskite materials such as Gd_2CoMnO_6 and Gd_2NiMnO_6, which also gives the scope for other rare earth–based double perovskites for similar effects (Brown 1976; Moon et al. 2017). $A_2BB'O_6$ is the general formula for these double perovskites, wherein the "A" site is occupied by rare-earth (divalent or trivalent) ions or alkaline-earth cations. Furthermore, the transition metal ion has 12-fold coordination in the B and B′ sites and exhibits an ideal octahedral coordinated orthorhombic structure.

The B and B′ sites play a main role in the origination of both the magnetic and electric ordering in the parent material (Zhong et al. 2004; Gheorghiu et al. 2015; Masrour and Jabar 2016). In Sr_2FeMoO_6, which is a well-known double perovskite material, the half-metallic ferromagnetic ordering and colossal magneto-resistance at room temperature have been observed simultaneously. As the oxygen ion cages contain either of the two transition metal cations (Mn/Ni) in the double perovskite structure in octahedral coordination, both the $Ni^{2+,}$ and Mn^{4-} ions assist in inducing the strong ferromagnetic superexchange (SE) interaction (Chandrasekhar et al. 2012). These materials tend to adopt two different types of crystal structures depending on the location of the Ni and Mn ions, i.e., if they are randomly arranged, they form the orthorhombic crystal structure with the Pbnm space group, and monoclinic structure with the space group of $P2_1/n$ if the arrangement is symmetric. Also ferromagnetism at low temperature for double perovskites is due to the anti-site defects occurred by interchange of B-site ions. This interchange in B-site crystallographic position is due to the variation in synthesis methods, annealing, controlled heating, and cooling rates at different atmospheres and also due to reduction of particle size to a nanometer scale, etc. (Chandrasekhar et al. 2012). Furthermore, double perovskite shows interesting spin glass (SG) behavior and spin glass transition like "freezing transitions" that show a state of new kind of spin order and produce long-range ferromagnetic (FM) or antiferromagnetic (AFM) ordering, which positively impacts the magnetocaloric effect (Su et al. 2018). Apart from the synthesis procedure, the crystal structures such as octahedral tilting of Ni/Mn–O, Ni–O–Mn bond length, and bond angles also play a great role in the magnetic exchange interaction.

The downturn of magnetization of Sm- and Nd-based systems is the cause of large crystalline anisotropy (due to spin-orbit coupling of Ni–Mn network rare earth); on the other hand, the same effect was not observed in the case of rare earth with larger moments such as Tb, Gd, Ho, and Dy (Tsui et al. 2017). This unusual behavior of Sm has been investigated before; however, no research work of its influence on the materials' magnetocaloric effect has been reported. In the present work, for the first time, novel Sm_2NiMnO_6 nanoparticles were prepared using a combustion technique, and its magnetocaloric properties were investigated for its application in magnetic refrigeration.

Experimental section

Sm_2NiMnO_6 nanoparticles were prepared via the solution combustion synthesis method. Samarium oxide (Sm_2O_3), manganese nitrate ($Mn(NO_3)_2$), and nickel nitrate ($Ni(NO_3)_2$) of > 99% purity were taken for the syntheses of Sm_2NiMnO_6 nanoparticles. A 2:1:1 molar mixture of Sm_2O_3, $Mn(NO_3)_2$, and $Ni(NO_3)_2$ was dissolved in distilled water, and dilute nitric acid (HNO_3) was added dropwise, to ensure the complete dissolution of all precursors. Finally, the combustion agent citric acid ($C_6H_8O_7$) was added to initiate the combustion process. The reaction mixture was kept on a preheated hot plate and stirred continuously using a magnetic stirrer for 2 h. After stirring, a black-colored powder was obtained that was ground for 10–15 min in a mortar

to get fine powders. The resulting mixture (black raw powder) was calcined at 700 °C for 4 h at a heating rate of 5 °C/min in a tube furnace under atmospheric conditions.

The phase analysis of as-synthesized Sm_2NiMnO_6 nanoparticles was performed using the powder X-ray diffraction (XRD) pattern obtained from Bruker D8 advance X-ray Diffractometer equipped with a Cu–Kα target ($\lambda1 = 1.5405$ Å) operating at 40 kV/40 mA and having a Bragg–Brentano geometry with fixed slits. The slow-scanned (step size: 0.02°, step time: 3 s) XRD pattern was Rietveld refined using the GSAS program with the EXPGUI graphical interface (Nederland 1969; Toby et al. 2001; Larson et al. 1994). The refined crystal structure was further illustrated using the DIAMOND 3.0 software (Pennington 1999). The morphology of the as-prepared Sm_2NiMnO_6 nanoparticles was analyzed using the JEM 2100 high-resolution transmission electron microscope (HRTEM) instrument operating at 200-kV accelerating voltage equipped with an EDAX analyzer. The selected area electron diffraction (SAED) pattern was captured by using a Gatan Orius CCD camera fixed within the JEM 2100 instrument. The magnetic measurements of Sm_2NiMnO_6 nanoparticles were acquired from the magnetic property measurement system (MPMS) equipped with the vibrating sample magnetometer. Magnetization as a function of temperature in the range of 2–300 K was probed in both the field-cooled (FC) and zero field–cooled (ZFC) mode with a constant external magnetic field of 100 Oe acquired. In the ZFC mode, the sample was cooled from 300 down to 2 K in the absence of any magnetic field. Subsequently, the desired external field was applied, and the data were collected on heating the sample up to 300 K. After reaching 300 K, the data record referred to as the FC mode was carried with the same strength of the field on cooling the sample down to 2 K.

Results and discussion

### Phase, structural, and microstructural characterization

The diffraction pattern obtained from the X-ray diffractometer at room temperature confirms the single phase from the Rietveld refinement carried out using the GSAS program as shown in Fig. 1. It shows the experimental and calculated pattern with the difference between their refined data and respective calculated Bragg positions; lattice parameters lie in the agreeable limit
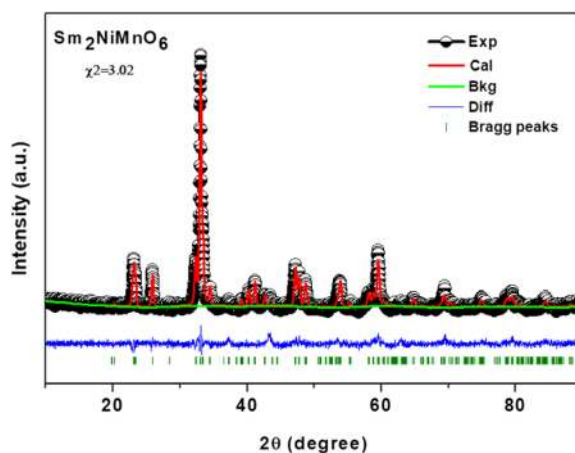
Fig. 1 Rietveld refinement of the synthesized Sm_2NiMnO_6 nanoparticles

when compared with the previous reports and the theoretically calculated values by the SPuDS program.

Sm_2NiMnO_6 refined using the monoclinic $P2_1/n$ space group (No. 11) with the ordered stacking of B-site ions resulted in satisfactory outputs rather than the orthorhombic $Pbnm$ space group. This confirms the centrosymmetric space group $P2_1/n$, which permits Ni/Mn ordering on the B sites (Booth et al. 2009; Shi et al. 2011; Snchez-Benítez et al. 2011). The rare-earth ions occupy 4e (x, y, z) sites in the lattice, while the oxygen atoms were found in three sites, namely, O1, O2, and O3. The remaining Ni and Mn atoms were positioned independently in 2d (0, 1/2, 0) and
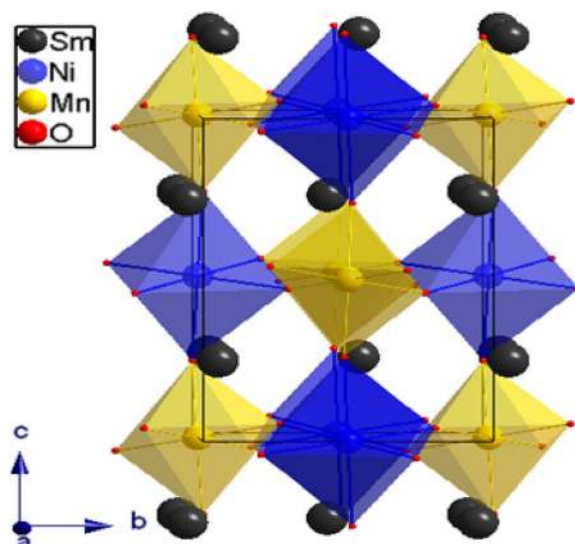
Fig. 2 Polyhedral representation of the unit cell of Sm_2NiMnO_6 compound viewed along the a-axis with blue and yellow octahedra that correspond to NiO_6 and MnO_6 octahedra respectively

Table 1 Crystallographic parameters of the Sm_2NiMnO_6 compound obtained from Rietveld refinement

Crystallographic parameters of Sm_2NiMnO_6	
Formula weight	510.3478
Crystal system	Monoclinic
Space group (No.)	$P2_1/n$ (14)
a (Å)	5.3522 (3)
b (Å)	5.5392 (4)
c (Å)	7.6126 (6)
β (°)	89.893 (12)
V (Å^3)	225.339 (1)
Z	2
Temperature (K)	293 (2)
wRp/Rp	0.0313/0.0229
Chi^2 value	3.795
Average bond angle (°) (Ni–O–Mn)	153.4

Table 3 Bond lengths (Å), bond valance sum (BVS) (left), and bond angles (right), obtained from Rietveld analysis of powder XRD data, of the Sm_2NiMnO_6 compound

Bond	Bond length (Å)	BVS
Ni–O(1) × 2	2.06	0.3337 × 2
Ni–O(2) × 2	1.98	0.4143 × 2
Ni–O(3) × 2	2.00	0.3925 × 2
BVS		2.29
Mn–O(1) × 2	1.84	0.7904 × 2
Mn–O(2) × 2	1.96	0.5715 × 2
Mn–O(3) × 2	1.99	0.5270 × 2
BVS		3.78
Bond angle (°)		
Ni–O1–Mn	154.6	
Ni–O2–Mn	155.5	
Ni–O3–Mn	149.9	
‹Ni–O–Mn›	153.4	

2c (1/2, 0, 0) sites, respectively. To compute the crystallographic parameters corresponding to the Sm_2NiMnO_6 structure, the DIAMOND 3.0 software was used, and Fig. 2 shows the crystal structure of the Sm_2NiMnO_6 compound. The structural data containing the complete crystallographic description of the compound and average bond valence sum (BVS) are listed in Table 1. BVS formalism was adapted to determine the individual Ni and Mn ion valence states. Effective valence (V_{ij}), the relation between the ith and jth atoms is given by $V_{ij} = \sum_j e^{\{(d_o - d_{ij})/0.37\}}$ where d_{ij}– is the bond length measure in between ith and jth atoms, and d_0– empirically determined bond valence parameter for the i–j pair (Su et al. 2018). The BVS indicates valence fluctuations between the Ni^{2+} (2.29) and Mn^{4+} (3.78) as calculated from their corresponding bond lengths (Ni–O and Mn–O). The values of atomic coordinates (Table 2), bond lengths, bond valence sums, and bond angles of Ni^{2+}–O–Mn^{4+} (Table 3) obtained as such from Rietveld analysis of the powder XRD data were tabulated.

Figure 2 shows the three-dimensional connection of the Sm_2NiMnO_6 structure, where the NiO_6 and MnO_6 octahedra are arranged. This displays the space group symmetry emerging from the combination of octahedral tilting similar to the Glazer tilt system (a−a−c+) and rock salt ordering of the octahedral cation as previously reported in double perovskites (Morrow et al. 2017). The tolerance factor has been calculated using the formula

$$t = \frac{r_R + r_O}{\sqrt{2\left[\frac{r_{Ni} + r_{Mn}}{2} + r_O\right]}}$$

where, r_R, r_{Ni}, r_{Mn}, and r_O are the effective ionic radii of R, Ni, Mn, and O ions respectively. The tolerance factor for the sample is found to be 0.921. From the literature, it can be observed that Sm_2NiMnO_6 nanoparticles show a tolerance factor lower than 0.97, which gives the distortions of perovskite structure from cubic symmetry and is in agreement with the $P2_1/n$ monoclinic symmetry (Serrate et al. 2007).

Table 2 Atomic coordinates and thermal parameters (Å^2), obtained from Rietveld analysis of powder XRD data, of the Sm_2NiMnO_6 compound

Atom	Site	x	Y	z	U_{iso} (Å^2)	Occupancy
Sm	4e	− 0.0139 (1)	0.05339 (3)	0.2500 (3)	0.0258 (1)	1
Ni	2c	0.500000 (0)	0.000000 (0)	0.500000 (0)	0.0265 (3)	1
Mn	2d	0.500000 (0)	0.000000 (0)	0.0000000 (0)	0.0245 (1)	1
O(1)	4e	0.078 (4)	0.4840 (3)	0.264 (1)	0.0440 (5)	1
O(2)	4e	0.719 (15)	0.275 (5)	0.047 (3)	0.0261 (4)	1
O(3)	4e	0.692 (1)	0.306 (1)	0.464 (2)	0.0260 (4)	1

Isofield and isothermal magnetization

The microstructure of Sm_2NiMnO_6 was studied using the HRTEM as shown in Fig. 3(a and b). The Sm_2NiMnO_6 nanoparticles obtained has an average particle size of about 60 nm. Furthermore, the lattice parameters were found to be about 0.369 nm as shown in Fig. 3(c). It also suggests that the orientation of Sm_2NiMnO_6 nanocrystallite is along the (110) plane. The results obtained from HRTEM are consistent with the analysis noted down from the diffraction pattern of XRD. The polycrystalline nature of Sm_2NiMnO_6 nanoparticles has been confirmed from the SAED as shown in Fig. 3(d).

The temperature-dependent ZFC and FC magnetization measurements were carried out for Sm_2NiMnO_6 nanoparticles as shown in Fig. 4(a). It can be seen that below 150 K, ZFC and FC curves bifurcate, and the
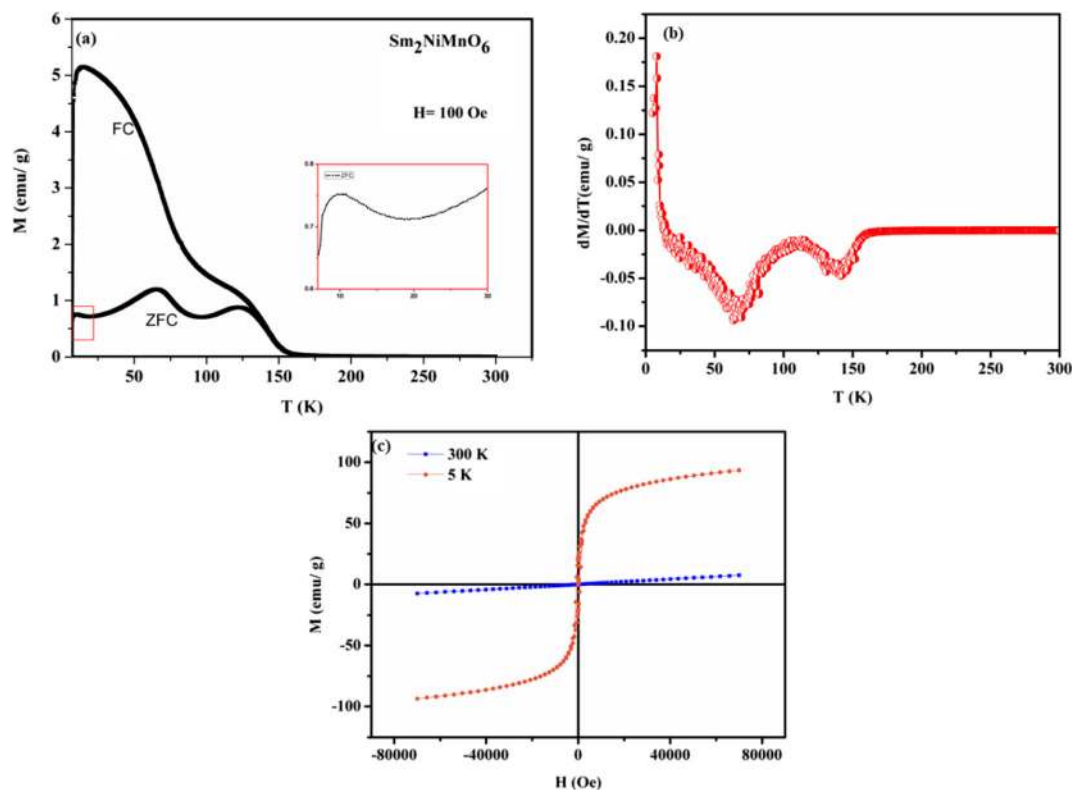
bifurcation point is termed as irreversible temperature (T_{irr}). The occurrence of combination of irreversible temperature with two anomalous peaks points towards the formation of frustrated FM phase in Sm_2NiMnO_6 nanoparticles at low temperature, which changes to paramagnetic phases on increasing the temperature above the Curie temperature. Two magnetic Curie transitions ($T_{C1} = 141$ K, $T_{C2} = 67$ K) corresponding to these broad maxima surfaced in the ZFC curve alongside its subsequent $T_{C2} = 152$ K in the FC curve. Such kind of behavior confirms the presence of ferromagnetism in the short range coupled with a paramagnetic behavior in the long range (Lekshmi et al. 2013). The dM/dT vs T plot from Fig. 4(b) shows the magnetic transition minima of the curves extracted from the derivative curves of the ZFC measurement. This spin ordering at low temperatures might be due to the spin reorientation caused by
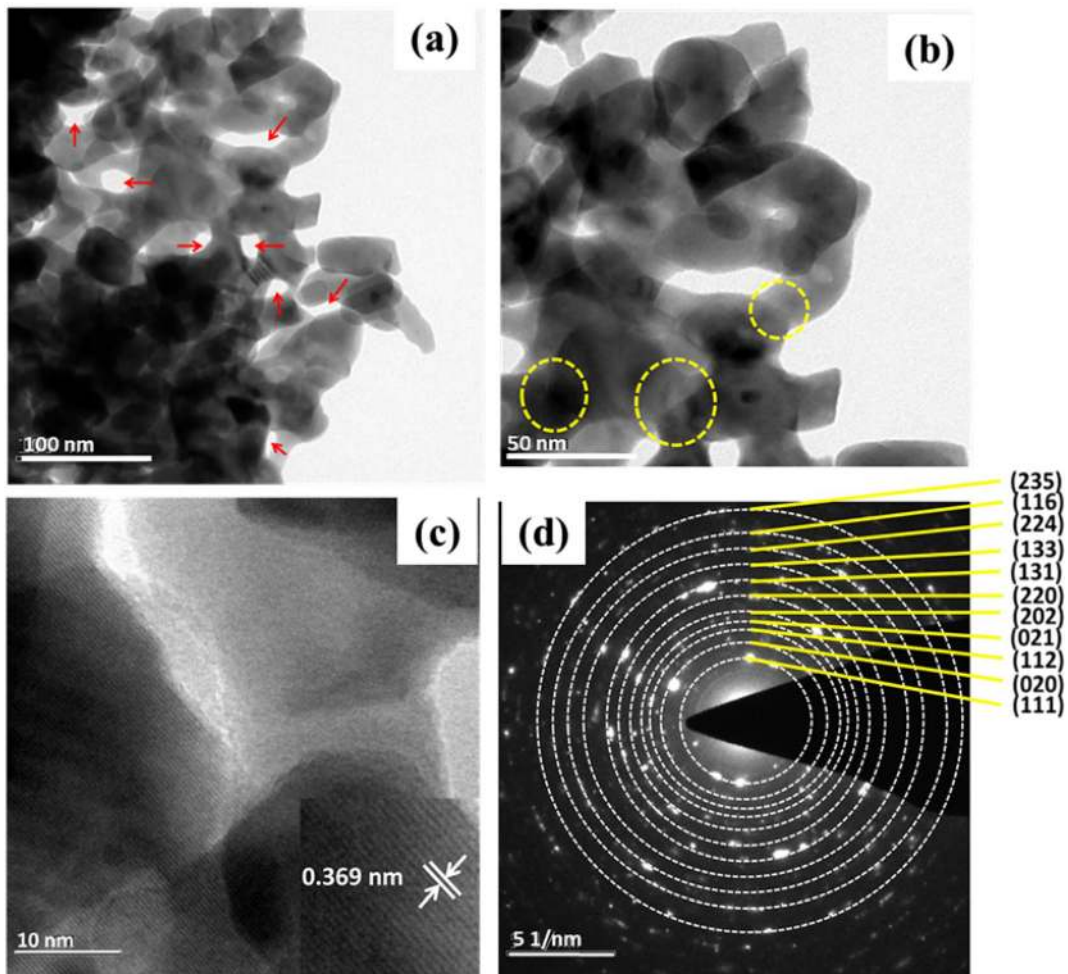
Fig. 3 HRTEM images. **a** 100 nm. **b** 50 nm. **c** Lattice distance indexed. **d** SAED pattern of the synthesized Sm_2NiMnO_6 with its corresponding (h k l) values

the uncompensated magnetic spins, which contributes to the weak ferromagnetic interactions. The magnetic field dependence of magnetic moments at 300 K and 5 K confirms the dominance of a weak ferromagnetic behavior at low temperatures as shown Fig. 4(c).

This weak ferromagnetic interaction at low temperatures might be due the valence fluctuations in the magnetic ordering of Ni^{2+}–O–Mn^{4+} as complemented by the calculated BVS from the X-ray diffraction pattern. This is analogous to the decrease in magnetization at low temperatures observed from the FC curves. Previous reports commend on the similar behavior in the Sm- and Nd-based Re_2NiMnO_6 systems, where the spin-orbit coupling inherent to the Mn–Ni matrix surrounding the R atoms could be due to the presence of magnetocrystalline anisotropy or the anti-site defects. Henceforth, the Sm^{3+} magnetic moment contribution is correlated with the magnetic ordering induced by the spin-orbit coupling phenomenon (Zhang et al. 2011; Yang et al. 2012). Besides the two magnetic transitions, a minor magnetic cusp can be observed from the ZFC curves at 10 K as shown in the Fig. 4a inset.

Magnetic phase transition

Full-range (30–170 K) isothermal measurement has been plotted as shown in Fig. 5(a) for studying the magnetocaloric effect in Sm_2NiMnO_6. In order to determine the order of magnetic phase transition occurring at the two magnetic transition ($T_{C1} = 141$ K, $T_{C2} = 67$ K), the magnetic isotherms were plotted between 170 and 130 K and 50 and 80 K successively as shown in Fig. 5(c and e). From the second derivative of Maxwell's equation,

$$M^2 = \frac{1}{4b}\frac{H}{M} - \frac{a\in}{2b}$$

(where, $\in = \frac{T-T_c}{T_c}$ is the dimensionless measure of temperature (T) in relation to critical transition temperature (T_c), "a" and "b" are material parameters), the corresponding Arrott plots (H/M vs M^2) were plotted as depicted in Fig. 5(b, d, and f).

The Arrott plot corresponding to the T_{N2} low-temperature regime shows a non-linear variation, which gives a negative slope, and that corresponding to the T_{N1} temperature regime shows a linear variation with a positive

Fig. 4 a Isofield ZFC–FC magnetization curves at the applied magnetic field 100 Oe. Inset: at 10 K. b The first derivative of the ZFC curve. c Magnetic isotherms at 5 K and 300 K for the synthesized Sm_2NiMnO_6

slope. It can be inferred from the Banerjee criterion that the former indicates the first-order magnetic phase transition and the latter presents a second-order transition. The major role of ferromagnetic interaction in Sm_2NiMnO_6 because of the superexchange interaction between Ni–O–Mn can

be confirmed from the linear fitting line cutting across in the positive x-axis from the positive slopes of the Arrott plot (Booth et al. 2009; Shi et al. 2011; Snchez-Benítez et al. 2011). The superexchange interaction occurs mainly between half-filled e_g electrons of Ni and
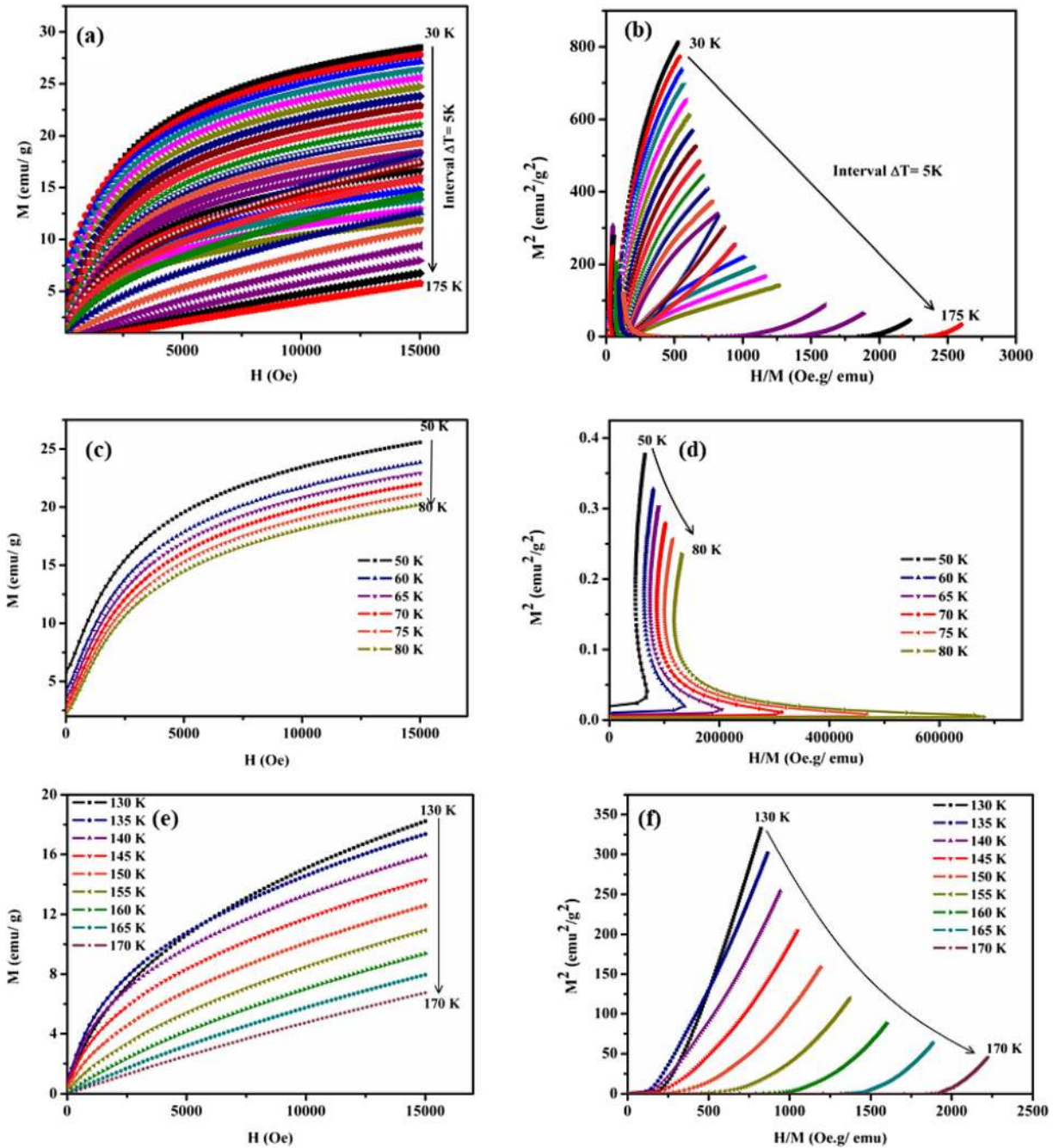
Fig. 5 Isothermal magnetization (M (emu/g)) vs magnetic field (H (Oe)) curves in the temperature range of a 30–175 K, and c 50–80 K, and e 130–170 K. Arrott plots of Sm_2NiMnO_6 nanoparticles

obtained by plotting M^2 (emu²/g²) Vs H/M (Oe.g/emu) for b 30–175 K, d 50–80 K, and f 130–170 K
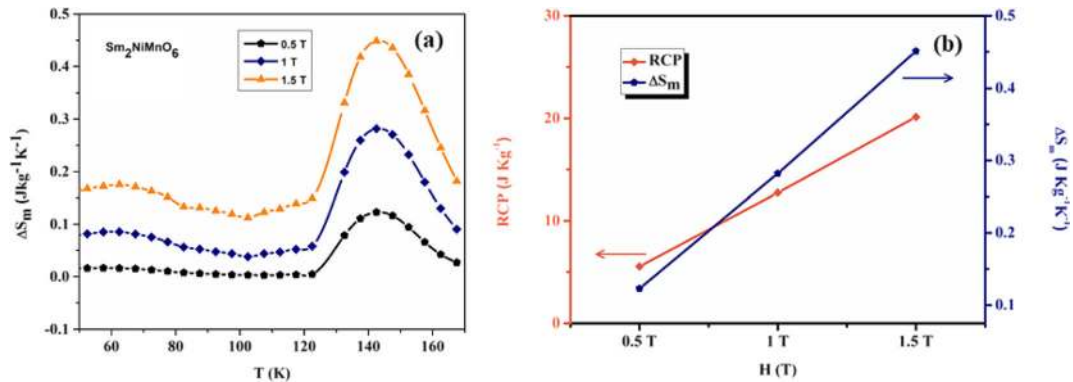
Fig. 6 **a** Temperature-dependent magnetic entropy change (ΔS_m) in the field range of 0.1 to 1.5 T. **b** Relative cooling power and linear plot of ΔS_m of the Sm_2NiMnO_6 nanoparticles

Mn, giving rise to ferromagnetic ordering (Das et al. 2008). Generally, the complexity of the Sm magnetism is given by anomalous magnetic ground state of the Sm^{3+} ion (Schmidt et al. 2015).

Magnetocaloric effect

The magnetocaloric properties of Sm_2NiMnO_6 in the T_{N2} temperature have been investigated by the estimation of magnetic entropy change (ΔS_m) using the Maxwell relation from the magnetic isotherms taken from 50 to 170 K. ΔS_m values determined from the magnetization–temperature relation at various applied fields are given by

$$\Delta S_m(T,H) = \int_0^{h_{max}} \left(\frac{\partial M}{\partial T}\right) H dH$$

From the above equation, it can be noticed that the values of (ΔS_m) depend on both values of M and ($\partial M/\partial T$) H. From ΔS_m vs T plot, the maximum entropy value of 0.44 J $kg^{-1}K^{-1}$ was obtained for the maximum applied field (1.5 T) as shown in Fig 6a. The relative cooling power (RCP) value can be calculated using the

formula RCP = $S \times T_{FWHM}$, where RCP is another important factor for assessing the capacity of the material to be used as a magnetic refrigerant. The RCP calculated was ~ 20 J kg^{-1}, and it depends not only on the magnitude of ΔS_m but also on the temperature dependence of ΔS_m, which is the full width at half maximum of the ΔS_m maxima as shown (Fig. 6b) in comparison tabulated in Table 4. For an applied field, the change in entropy increases with increase in temperature up to a certain temperature, and then it decreases. The peak change in entropy value decreases on increasing the applied field. This suggests that on increasing the field, the frustrated FM phase decreases its randomness.

Chakraborty et al. (2017b) have explained that variation of ΔS_m does not follow any common trend when compared with M or μ_{eff} of the samples. The ΔS_m and RCP values obtained for Sm_2NiMnO_6 are less than any other double perovskite manganites. The value of ΔS_m (0.44 J kg^{-1} K^{-1}) at T_c (T_{C2} = 141 K) is due to adiabatic magnetization of the material, which can be well-suited as a magnetic refrigerant at cryogenic temperatures. The magnetic entropy change is also correlated with the spin lattice coupling in the presence of a magnetic field as it increases along the

Table 4 Comparison of entropy T_c (K) and RCP of the synthesized Sm_2NiMnO_6 with the literature

Compound name	T_c (K)	ΔS_m J/kg K @ H	RCP J/kg	References
Sm_2NiMnO_6	141	0.44@1.5T	20.1	This work
Y_2NiMnO_6	81	2.9@2T	74.88 [1]	Chakraborty et al. 2017a
Pr_2NiMnO_6	213	2.4@2T	41.35 [1]	Chakraborty et al. 2017a
Tb_2NiMnO_6	110	2.4@2T	52.49 [1]	Chakraborty et al. 2017a
Nd_2NiMnO_6	191	1.1@2T	24.05 [1]	Chakraborty et al. 2017a
Dy_2NiMnO_6	101	3.4@7T	169 [27]	Law et al. 2018
Ho_2NiMnO_6	93	3.7@7T	194 [27]	Law et al. 2018
Er_2NiMnO_6	84	3.4@7T	169 [27]	Law et al. 2018

applied field. The applied magnetic field and magnitude of exchange interaction between Mn and Ni ions play an important role in the values of the parameters related to the magnetocaloric effect (MCE).

The role of structural defect in the MCE can be shown by the coercive field of this double perovskite. The structural defects such as anti-phase boundaries acting as domain pinning centers can be very important in such highly anisotropic compounds. Here, the anti-phase boundaries form a plane consisting of antiferromagnetic superexchange interaction between Mn and Ni ions over oxygen ions in both B and B′ sites. This can be confirmed when there is a shift in lattice, which is equal to half a lattice parameter (Law et al. 2018; Kim et al. 2019). The external large magnetic entropy change may be attributed to a large number of weakly interacting spins. This inference indicates that the material is a promising magnetocaloric refrigerant candidate for low-temperature application and possibly could make ultra-low temperatures easily achievable for most laboratories as well as space applications.

Conclusion

Monoclinic double perovskite Sm_2NiMnO_6 nanoparticles synthesized via the solution combustion technique were found to have valence fluctuations (Ni^{2+}–O–Mn^{4+}) as observed from the BVS values calculated from the Rietveld-refined XRD pattern, which contributed to the short-range ferromagnetic behavior. Two magnetic Curie transitions ($T_{C1} = 141$ K, $T_{C2} = 67$ K) were observed exhibiting their respective second-order and first-order magnetic phase transition from the Arrott plot, revealing the long-range paramagnetic ordering of spins. Furthermore, the magnetic entropy caused by the adiabatic demagnetization of Sm_2NiMnO_6 nanoparticles was calculated to be 0.44 J kg^{-1} K^{-1} for the maximum applied field (1.5 T) at 141 K, and its corresponding magnetic refrigeration capacity was ~ 20 J kg^{-1}. The suppressed magnetic entropy values compared with the other rare-earth double perovskite manganites were due to the dominance of short-range ferromagnetic ordering of the magnetic spins along with multiple orders of magnetic phase transition across the 10–170 K range. Yet, this is an interesting phenomenon extending the scope of further exploring the wide range of switching magnetic transition from low to high magnetic applied fields, which could be used in the case of layered magnetic refrigeration. Furthermore, the complementary magnetic dielectric and magnetic resistance behaviors inherent to the $SmNiMnO_6$ could be considered as an excellent multifunctional material.

References

Booth RJ, Fillman R, Whitaker H, Nag A, Tiwari RM, Ramanujachary KV, Gopalakrishnan J, Lofland SE (2009) An investigation of structural, magnetic and dielectric properties of R_2NiMnO_6 (R = rare earth, Y). Mater Res Bull 44: 1559–1564. https://doi.org/10.1016/j.materresbull.2009.02.003

Brown GV (1976) Magnetic heat pumping near room temperature. J Appl Phys 47:3673–3680. https://doi.org/10.1063/1.323176

Chakraborty T, Nhalil H, Yadav R, Wagh AA, Elizabeth S (2017a) Magnetocaloric properties of R_2NiMnO_6 (R=Pr, Nd, Tb, Ho and Y) double perovskite family. J Magn Magn Mater 428:59–63. https://doi.org/10.1016/j.jmmm.2016.12.015

Chakraborty T, Nhalil H, Yadav R, Wagh AA, Elizabeth S (2017b) Magnetocaloric properties of R_2NiMnO_6 (R=Pr, Nd, Tb, Ho and Y) double perovskite family. J Magn Magn Mater 428:59–63. https://doi.org/10.1016/j.jmmm.2016.12.015

Chandrasekhar KD, Das AK, Mitra C, Venimadhav A (2012) The extrinsic origin of the magnetodielectric effect in the double perovskite La_2NiMnO_6. J Phys Condens Matter 24:495901. https://doi.org/10.1088/0953-8984/24/49/495901

Das H, Waghmare UV, Saha-Dasgupta T, Sarma DD (2008) Electronic structure, phonons, and dielectric anomaly in ferromagnetic insulating double pervoskite La_2NiMnO_6. Phys Rev Lett 100:1–4. https://doi.org/10.1103/PhysRevLett.100.186402

El Kossi S, Ghodhbane S, Mnefgui S et al (2015) The impact of disorder on magnetocaloric properties in Ti-doped manganites of $La_{0.7}Sr_{0.25}Na_{0.05}Mn_{(1-x)}Ti_xO_3$ (0≤x≤0.2). J Magn Magn Mater 395:134–142. https://doi.org/10.1016/j.jmmm.2015.07.050

Gheorghiu F, Curecheriu L, Lisiecki I, Beaunier P, Feraru S, Palamaru MN, Musteata V, Lupu N, Mitoseriu L (2015) Functional properties of Sm_2NiMnO_6 multiferroic ceramics prepared by spark plasma sintering. J Alloys Compd 649: 151–158. https://doi.org/10.1016/j.jallcom.2015.07.136

Kim MK, Moon JY, Oh SH, et al (2019) Strong magnetoelectric coupling in mixed ferrimagnetic-multiferroic phases of a double perovskite. 1–10. https://doi.org/10.1038/s41598-019-41990-9

Kotnana G, Babu PD, Jammalamadaka SN (2018) Magnetic and magnetocaloric properties of $HoCr_{0.75}Fe_{0.25}O_3$ compound magnetic and magnetocaloric properties. https://doi.org/10.1063/1.5006562

Larson AC, Von Dreele RB (2004) General Structure Analysis System (GSAS). Los. Alamos National Laboratory Report LAUR, New Mexico, pp 86–748

Law JY, Franco V, Moreno-Ramírez LM, Conde A, Karpenkov DY, Radulov I, Skokov KP, Gutfleisch O (2018) A quantitative criterion for determining the order of magnetic phase transitions using the magnetocaloric effect. Nat Commun 9:2680. https://doi.org/10.1038/s41467-018-05111-w

Lekshmi PN, Raji GR, Vasundhara MV, Manoj RP, Savitha S, Valant M (2013) Re-entrant spin glass behaviour and magneto-dielectric effect in insulating Sm_2NiMnO_6 double perovskite. J Mater Chem C 1:6565. https://doi.org/10.1039/c3tc31203h

Masrour R, Jabar A (2016) Magnetocaloric and magnetic properties of La_2NiMnO_6 double perovskite. Chinese Phys B 25:2–8. https://doi.org/10.1088/1674-1056/25/8/087502

Moon JY, Kim MK, Choi YJ, Lee N (2017) Giant anisotropic magnetocaloric effect in double-perovskite Gd_2CoMnO_6 single crystals. Sci Rep 7:1–10. https://doi.org/10.1038/s41598-017-16416-z

Morrow R, Mcguire MA, Yan J, Woodward PM (2017) The crystal structure and magnetic behavior of quinary osmate and ruthenate double perovskites $LaABB'O6$(A= Ca, Sr;B= Co, Ni;B′ = Ru, Os). 57(6):–3001. https://doi.org/10.1021/acs.inorgchem.7b02282

Nederland RC (1969) A profile refinement method for nuclear and magnetic structures. https://doi.org/10.1107/S0021889869006558

Pennington WT (1999) DIAMOND–visual crystal structure information system. J Appl Crystallogr 32:1028–1029. https://doi.org/10.1107/s0021889899011486

Romero Gómez J, Ferreiro Garcia R, De Miguel CA, Romero Gómez M (2013) Magnetocaloric effect: a review of the thermodynamic cycles in magnetic refrigeration. Renew Sust Energ Rev 17:74–82. https://doi.org/10.1016/j.rser.2012.09.027

Schmidt M, Zimmer FM, Magalhaes SG (2015) Weak randomness in geometrically frustrated systems: spin-glasses. Phys Scr 90:25809. https://doi.org/10.1088/0031-8949/90/2/025809

Serrate D, De Teresa JM, Ibarra MR (2007) Double perovskites with ferromagnetism above room temperature. J Phys Condens Matter 19:0–86. https://doi.org/10.1088/0953-8984/19/2/023201

Shi C, Hao Y, Hu Z (2011) Local valence and physical properties of double perovskite Nd_2NiMnO_6. J Phys D Appl Phys 44:245405. https://doi.org/10.1088/0022-3727/44/24/245405

Snchez-Benítez J, Martínez-Lope MJ, Alonso JA, García-Mũoz JL (2011) Magnetic and structural features of the $NdNi_{1-x}Mn_xO_3$ perovskite series investigated by neutron diffraction. J Phys Condens Matter 23. https://doi.org/10.1088/0953-8984/23/22/226001

Su L, Zhang X-Q, Dong Q-Y, Ke YJ, Hou KY, Liu CS, Cheng ZH (2018) Magnetocaloric effect and critical behaviors of R_2NiMnO_6 (R=Eu and Dy) double perovskite oxides. J Alloys Compd 746:594–600. https://doi.org/10.1016/j.jallcom.2018.02.327

Takeuchi I, Sandeman K (2015) Solid-state cooling with caloric materials. Phys Today 68:48–54. https://doi.org/10.1063/PT.3.3022

Toby BH (2001) EXPGUI, a graphical user interface for GSAS. J Appl Cryst 34:210. https://doi.org/10.1107/S0021889801002242

Tsui MHM, Dryer DT, El-Gendy AA, Carpenter EE (2017) Enhanced near room temperature magnetocaloric effect in $La_{0.6}Ca_{0.4}MnO_3$ for magnetic refrigeration application. RSC Adv 7:46589–46593. https://doi.org/10.1039/c7ra06619h

Yang WZ, Liu XQ, Zhao HJ, Lin YQ, Chen XM (2012) Structure, magnetic, and dielectric characteristics of Ln_2NiMnO_6 (Ln= Nd and Sm) ceramics. J Appl Phys 112:0–6. https://doi.org/10.1063/1.4752262

Zhang G, Li G, Liao F, Fu Y, Xiong M, Lin J (2011) Crystal growth and magnetic properties of the double perovskites R_2MnNiO_6 (R= Pr, Sm and Ho) by a hydrothermal route. J Cryst Growth 327:262–266. https://doi.org/10.1016/j.jcrysgro.2011.06.002

Zhong W, Liu W, Wu XL, Tang NJ, Chen W, Au CT, du YW (2004) Magnetocaloric effect in the ordered double perovskite $Sr_2FeMo_{1-x}W_xO_6$. Solid State Commun 132:157–162. https://doi.org/10.1016/j.ssc.2004.07.060